UC Berkeley
UC Berkeley Previously Published Works

Title
Hierarchical Thiospinel NiCo2S4/Polyaniline Hybrid Nanostructures as a Bifunctional Electrocatalyst for Highly Efficient and Durable Overall Water Splitting

Authors
Garain, Samiran
Van, Cu Dang
Choi, Seungwoo
et al.

Hierarchical Thiospinel NiCo2S4/Polyaniline Hybrid Nanostructures as a Bifunctional Electrocatalyst for Highly Efficient and Durable Overall Water Splitting

Samiran Garain, Cu Dang Van, Seungwoo Choi, Tru Nguyen Dang, Joel W. Ager, Ki Tae Nam, Hyeyoung Shin,* and Min Hyung Lee*

Dr. S. Garain, C. Dang Van, T. Nguyen Dang, Prof. M. H. Lee
Department of Applied Chemistry, Kyung Hee University, Yongin, Gyeonggi 17104, Republic of Korea.
E-mail: minhlee@khu.ac.kr

S. Choi, Prof. K. T. Nam
Department of Materials Science and Engineering, Seoul National University, Seoul 08826, Republic of Korea.

Prof. J. W. Ager
Department of Materials Science and Engineering, University of California, Berkeley, California 94720, United States.
Materials Sciences Division and Joint Center for Artificial Photosynthesis, Lawrence Berkeley National Laboratory, Berkeley, California 94720, United States.

Prof. H. Shin
Graduate School of Energy Science and Technology (GEST), Chungnam National University, Daejeon 34134, Republic of Korea.
E-mail: shinhy@cnu.ac.kr

The development of a nonprecious, stable, and highly efficient electrocatalyst for decomposition of water into oxygen and hydrogen is vitally important for sustainable energy conversion, but it still remains challenging to replace the noble metal electrocatalysts with more economically viable alternatives. Herein, we have judiciously designed and developed a polyaniline (PANI) decorated hierarchical nickel cobalt thiospinel (NiCo2S4) hybrid catalyst (NCS-P) that shows enhanced electrocatalytic activity for both the oxygen evolution reaction (OER) and the hydrogen evolution reaction (HER) compared to nondecorated NiCo2S4 (NCS). Benefiting from the conductive PANI coating, the hierarchical NCS-P nanostructure exhibits

outstanding electrocatalytic activity in alkaline solution with small overpotentials of 273±3 mV and 77±4 mV to achieve a current density of 10 mA cm^{-2} and Tafel slopes of 42.2 and 68.5 mV dec-1 for OER and HER, respectively, which are better than that of the benchmark noble-metal-based RuO2 catalyst and comparable to that of commercial Pt/C.

1. Introduction

In order to solve or relieve the increasing energy demands, ever worsening global warming, and fossil fuel depletion problems, the development of eco-friendly, renewable, and alternative clean energy resources for the efficient sustainable energy is highly required.[1] As an alternative to the conventional fossil fuels, hydrogen is considered as a promising renewable future energy source for overcoming the energy depletion because of its super-high calorific value (~1.4×108 J/kg), high energy conversion efficiency, and environmentally friendly energy source with ecological impact.[2] Renewable energy driven electrochemical water splitting into high purity hydrogen and oxygen has been attracting more attentions for producing clean sustainable and green energy infrastructure to ameliorate the environmental energy issues.[3]

The thermodynamic potential to drive water splitting is 1.23 V. However, the requirement of high overpotential to electrochemically split water into H2 and O2 is an overriding limitation, and thus the development of highly active and durable catalysts is of great importance to reduce the additional energy expenditure.[4] Nowadays, the most efficient electrocatalysts are based on noble metal materials, e.g., RuO2/IrO2 for OER and Pt-based catalysts for HER, respectively.[5] Due to their scarcity, high cost, and low bifunctionality (i.e., high catalytic performance for both OER and HER), the utilization of these noble metal-based catalysts should be drastically reduced in order to make large-scale applications realistic. Great effort has been devoted towards developing effective, earth abundant, and stable non-noble-metal based low-cost OER and HER electrocatalysts. Among them three-dimensional (3D) transition metal-

based catalysts, such as carbides, oxides, nitrides, phosphides, and sulfides for HER, as well as oxide/hydroxides for OER have been considered as the promising electrocatalysts for water splitting because of their high catalytic activity which can be developed by precise control of their composition and morphology.[6-8]

However, the HER catalysts are more efficient in acidic solutions, while most of the OER catalysts are reported to have an enhanced catalytic ability in alkaline electrolytes compared to acid media. For the sake of cost-effectiveness and practical consideration, the development of a promising bifunctional electrocatalysts simultaneously catalyzing the OER and the HER in the same electrolyte is extremely desirable and remains challenging. Accordingly, we have been motivated to design highly active, durable, and inexpensive novel bifunctional electrocatalysts that are equally effective for both HER and OER while being in the same electrolyte.

Among all the approaches under investigation, constructing electrocatalysts with heteroatom system was regarded as an efficient method to remarkably improve the electrocatalytic activities of the OWS through the coupling synergistic interplay of different elements which could tune the electronic structure and exposure of increased catalytic active sites.[9] However, the common Co-based electrocatalysts suffer from an inferior HER performance due to the limited number of active sites to boost all steps in the HER process.[10] To address this problem, researchers have introduced several heteroatoms (e.g., Mo, Fe, Pd, Ni, and P) into the Co-based catalysts leading to the production of numerous active sites and then the enhancement of electrocatalytic performances.[10-13] Particularly, Ni-Co bimetallic electrocatalysts have been extensively explored, with some reports of superior OWS performance in an alkaline electrolyte.[12, 14] Recently, Ni-Co based oxides have been widely explored as OER electrocatalysts on various supports.[1, 15] Most of the Ni-Co based materials reported to date have not been active for OWS (e.g., both OER and HER) in the same electrolyte environment because of their poor intrinsic conductivity and deficient concentration of active sites, hampering their applicability in the OWS process.[16] Bimetallic (Ni-Co) sulfides (NCS) with

spinel structure have attracted attention as a prospective non-noble metal electrocatalyst for OWS, benefiting from its very high electronic conductivity (~100 times higher than that of NiCo2O4) than its oxide/hydroxide counterparts.[14] In recent years, hierarchical nanostructures composed of either geometric complexity or multiple constituents have drawn great interest. Zhao et al. demonstrated hierarchical NiFe/NiCo2O4 nanostructure by electrodeposition method as bifunctional catalysts, which showed highly efficient whole cell water splitting.[17]

Specifically, the high conductivity and electroactive properties of the electrocatalyst make them be able to catalyze the redox reactions.[18] Furthermore, coating with conducting polymers is also a wise strategy to solve the issue of conductivity. Among conducting polymers, PANI is one of the most extensively studied conducting polymers because of its unique one dimensional delocalized conjugated structures and attractive traits, such as light weight, good electroactive properties, high conductivity, mechanical flexibility, and low cost.[18-19] Moreover, PANI has various anchor sites for metal ions due to the presence of numerous amino groups, preventing metal nanoparticles (NPs) from aggregation to expose more active sites. Meanwhile, PANI can also interact with electrocatalysts and thus modulate the electronic structure of the catalysts.[19] The resultant unique structure with integrated hierarchical configuration can enhance the mass transport and charge mobility, and facilitate the diffusion of the generated H2 and O2 gases.

Motivated by the above considerations, herein, we preferably choose PANI as the conducting polymer for functionalization of hierarchical thiospinel NCS NPs to achieve high performance OWS by tuning the surface electronic structures with an enhanced charge transfer ability. Through structural studies, we confirmed the successful formation of the thiospinel NCS NPs and X-ray photoelectron spectroscopy (XPS) peaks revealing the existence of multiple oxidation states of the active species in the crystal structure and the strong electronic interactions between NCS NPs and PANI. Coating with the conductive PANI was found to

4

efficiently improve the bifunctional electrocatalytic performance for both OER and HER of the NCS catalyst. Various systematic experiments and theoretical analysis display that the as-formed PANI/NCS hybrid can fully utilize the advantages of NCS, PANI, and their strongly coupled heterointerface for achieving highly efficient intrinsic OWS performance. The high mass activity, excellent conductivity, high surface area, and outstanding robustness of the PANI/NCS hybrid material enable to achieve superior electrocatalytic activity for both OER and HER with excellent durability in 1.0 M KOH electrolyte solution, which are comparable to the state-of-the-art catalysts RuO_2 and Pt/C, respectively. Furthermore, the PANI/NCS hybrid catalyst used as both anode and cathode electrodes and show remarkable activity toward OWS to achieve a current density of 10 mA cm^{-2} at a very low cell voltage of 1.582 V in 1.0 M KOH with high energy efficiency of ~80% as well as long-term stability.

2. Results and discussion

2.1. Synthesis and characterization of NCS-P

The preparation of the NCS-P hybrid electrocatalyst was realized by hydrothermal process in a facile and scalable strategy by using cobalt(II) nitrate hexahydrate ($Co(NO_3)_2 \cdot 6H_2O$) and nickel(II) nitrate hexahydrate ($Ni(NO_3)_2 \cdot 6H_2O$) as metal precursors and urea as reducing hydrolysis agent to generate $NiCo_2(OH)_6$, which is further experienced a sulphidation treatment at 150 °C in the presence of sodium sulfide nonahydrate ($Na_2S \cdot 9H_2O$) to form NCS (Scheme 1a). The NCS-P was obtained by dispersing NCS and PANI in ethanol with intense ultra-sonication and stirring (Scheme 1b) (see the Experimental Methods for details).

To investigate the cardinal ingredient phases and purity of the as-prepared hybrid electrocatalysts, XRD analysis was carried out and the result was exhibited in Figure 1a. The diffraction peaks at values of 2θ of 26.9°, 31.5°, 38.2°, 50.4°, and 55.2° can be assigned to the (220), (311), (400), (511), and (440) planes, respectively, of NCS having cubic spinel phase (Scheme 1c) with a space group of Fd3m (JCPDS card No. 20-0782). The diffraction peaks in

Figure 1a confirm the successful formation of a cubic NCS phase without any impurities. For comparison, Ni3S2 (NS) was synthesized by a similar process to that of the preparation of NCS. The peaks at 21.8, 31.2, 38.8, 49.6 and 55.1° corresponding to (101), (110), (021), (113) and (122) planes of rhombohedral Ni3S2 phase (JCPDS card No. 44-1418), respectively (Figure S1b). The characteristic peaks observed in as-prepared sample confirmed the formation of Ni3S2. However, no diffraction peak of PANI is observed in PANI coated NCS (NCS-P) and PANI coated NS (NS-P) due to its low amount and relatively low diffraction intensity (Figure 1a and Figure S1b). In order to verify the presence of PANI, NCS-P hybrid was further examined by EDS and XPS analysis.

Surface morphologies of NCS and NCS-P were characterized by field emission-scanning electron microscopy (FE-SEM). As shown in Figure 1c, the NCS NPs are uniformly distributed within PANI without aggregation. This uniform distribution of the NCS may mean the full exposure of catalytic active sites. However, NCS nanoparticles without PANI have a remarkable aggregation (Figure 1b), which can hinder the exposure of catalytic active sites. The particle size of NCS-P is smaller (average particle size ~ 26.5 nm) than that of NCS (average particle size ~ 44.5 nm) as shown in the inset of Figure 1c and 1b, respectively. This may be related to the support of PANI and indicates that PANI is key to suppress particle aggregation and obtain the small-sized NCS-P catalyst. This unique structure would provide a large electrochemically active surface area that could readily access electrolyte ions and increase the number of active sites for OER and HER.

A similar morphology was observed for NCS-P using transmission electron microscopy (TEM) as shown in Figure 1d. The NCS having cubic spinel lattice planes indexed in XRD could be readily found in the selected area electron diffraction (SAED) pattern of NCS-P (Figure 1e). The diffraction rings in the SAED pattern can be readily indexed to the (311), (400), (511) and (440) planes of a cubic phase of NCS, which is consistent with the XRD result.[30] Figure 1f is a high-resolution TEM (HRTEM) image of NCS-P. The distance

6

between lattice fringes can be found to be 0.234 nm and 0.283 nm, which are related to the (400) and (311) planes of NCS (JCPDS No. 20-0782), respectively. However, there is an amorphous component wrapping the outside of the NCS in Figure 1f, demonstrating that the PANI is successfully covered on the NCS. The SAED pattern and HRTEM result are in good agreement with the XRD results which support the abovementioned conclusion that the as prepared electrocatalyst is pure NCS. The regional EDS spectra and EDS elemental mapping images revealed the superposition of the uniform spatial distribution of the Ni, Co, S, and N over the examined detection range at the surface of the NCS-P (Figure S2, and Figure 1g–k). The existence of the N element further indicates that the PANI have been functionalized with NCS (Figure 1k), indicating that the NCS/PANI hybrid was successfully prepared.

To obtain the chemical valence state and the surface chemical composition of the various elements in the NCS-P hybrid catalyst, X-ray photoelectron spectra (XPS) were analyzed using the Gaussian fitting method (Figure 2a-e). The presence of Ni, Co, S, C, and N elements can be facilely observed in the surface survey spectrum of NCS-P in Figure S3. The element O may come from absorbed CO_2 in air or the partial oxidation of metal sulfide at the surface Ni^{2+} when exposed to air.[20] In Ni 2p region (Figure 2a), the binding energies at ~855.9 eV for Ni 2p1/2 Ni 2p3/2 and ~873.4 eV for Ni 2p1/2 are spin-orbit characteristics of Ni^{2+}, while the existing binding energies appear at ~857.4 eV for Ni 2p3/2 and ~875.3 eV for Ni 2p1/2 are spin-orbit characteristics of Ni^{3+}. This indicates the co-existence of Ni^{3+} and Ni^{2+}.[21] Similar to previous reports, an intense satellite peak (marked as 'Sat.' in Figure 2a) suggested that the Ni^{2+} state was predominant in the Ni 2p spectra.[22] The Co 2p XPS spectrum (Figure 2b) is similar to the Ni 2p, where two kinds of cobalt species containing Co^{3+} and Co^{2+} can be observed. The binding energies at ~780.9 eV (2p3/2) and ~796.8 eV (2p1/2) of the Co 2p peaks indicate the existence of Co^{3+}, while the binding energies at ~782.5 eV (2p3/2) and ~798.4 eV (2p1/2) are the characteristic of Co^{2+}, also indicating the co-existence of Co^{3+} and Co^{2+} in NCS-P hybrid catalyst.[21] Besides, the peaks centered at ~778.6 eV and 793.8 eV

reflects the existence of Co–O bond due to the partial oxidation of metal sulfide, which is consistent with the appearance of oxygen in survey spectrum above. The Co 2p XPS spectrum (Figure 2b) is similar to the Ni 2p, where the binding energies at ~781.4 eV (2P3/2), ~797.4 eV (2P1/2) and ~778.5 eV (2P3/2), ~793.6 eV (2P1/2) are most likely corresponded to Co2+ and Co3+, respectively, indicating the co-existence of Co3+ and Co2+ in NCS-P hybrid catalyst.[21] The S 2p spectrum was deconvoluted into four peaks ascribed in Figure 2c. The binding energies at ~161.5 and ~162.9 eV correspond to the spin-orbit coupling values of S 2p3/2 and S 2p1/2, respectively, which are related to S2- ions of the NCS compounds. The component peaks at ~168.5 eV and ~169.7 eV is are associated with the satellite peaks. binding energy of a metal–sulfur (Ni–S and Co–S) bond in the NCS-P, while the other component peak present at ~161.7 eV attributed to the presence of sulfur ions (S-2) in a low coordination state at the surface.[23] According to the XPS analysis, the surface of NCS-P has a composition of Ni2+, Ni3+, Co2+, Co3+, and S2−, which is in good agreement with the previous reports.[22-23] This result is consistent with the formation of spinel NCS phase, as revealed through XRD analysis (Figure 1a).

Furthermore, the C 1s XPS spectrum (Figure 2d) shows the presence of four different types of carbon species with the binding energies at ~284.6, ~285.5, ~286.57 and 288.6 eV representing the C=C, C–NH, C=N, and C–O or C=O bonds in PANI, respectively.[23] In addition, the N1s spectrum can be further deconvoluted into three characteristic nitrogen bonding environments of benzenoid amine-like structure (–NH–) at ~399.2 eV, quinoid imine-like structure (–C=N–) at ~399.9 eV, and the generated iminium ions (–N+H–) at 401.1 eV, respectively, as shown in Figure 2e, which implies that the NCS was successfully decorated by PANI. The highest binding energy peak observed in N+ is due to the protonated amine units.[24]

To further analyze the interactions between NCS and PANI, XPS can be utilized to investigate the electronic structures of NCS and PANI in NCS-P so that the interactions can be clarified. The high-resolution XPS spectra for Ni 2p, Co 2p of both NCS and NCS-P and N 1s

of both NCS-P and PANI are compared in Figure 3. While the binding energies of Ni and Co for the NCS-P are shifted to higher energy by 0.4 and 0.3 eV compared to those of NCS, respectively, the binding energy of N for the NCS-P is shifted to lower energy by 0.17 eV compared to that of PANI, suggesting the electronic interactions between NCS and PANI in the NCS-P. The observed shifts in the binding energies might imply the possible electron delocalization from d-orbital of Ni and Co to π-conjugated structure of PANI.[19, 24-25] The electronic interactions not only facilitate the formation of high valence metal sites that can be the active sites for OER but also accelerate the generation of intermediates during OER process.

The relative atomic ratio (Ni3+/ Ni2+) on the surface of both NCS and NCS-P could be obtained by comparing the area of the fitted curves. The ratio of the peak area of Ni3+/ Ni2+ in the Ni 2p spectrum on the surface of NCS-P is notably higher (Ni3+/ Ni2+ = 8.38) than that of the NCS (Ni3+/ Ni2+ = 2.47) (Figure S4a), indicating the strong electronic coupling between NCS and PANI in NCS-P. Simultaneously, the introduction of PANI could give rise to a small electron transfer from Ni to PANI due to the electron acceptability and the surface of NCS easily oxidized to form the OER active Ni3+ or Ni4+ species (Figure 2f).[23] The binding energies of Co3+ in Co 2p3/2 and 2p3/2 peaks for the NCS-P are negatively shifted (~0.7 eV for Co 2p3/2 and ~0.6 eV for Co 2p1/2) to a lower binding energy compared with that of the pristine NCS as shown in Figure 3a and 3b. Figure 3c shows that the −N+− characteristic peak of NCS-P exhibits a positive shift of ~1.1 eV to the higher binding energies compared with those of PANI, which also confirms the existence of strong electronic interactions involving NCS and PANI in the NCS-P.[18] Moreover, the ratio of the peak area of Co3+ to Co2+ (Co3+/ Co2+) in the Co 2p spectrum for NCS-P was estimated to be 0.21, much smaller than that of the pristine NCS (Co3+/ Co2+ = 0.82), which also confirms to the fact that NCS can harvest electrons from PANI and at the same time Co3+ partially converted into Co2+ (Figure S4b) so that it will be beneficial for electron transport during HER.[19] Figure 3c shows that the −N+− characteristic peak of NCS-P exhibits a positive shift of ~1.1 eV to the higher binding energies

compared with those of PANI. The observed shift in binding energies implies the partial electron transfer from PANI to NCS through the strong electronic coupling.

2.2. Electrocatalytic activity of NCS-P toward OER

   The OER performance was carried out in O2-saturated 1.0 M KOH electrolyte with the NS, NCS, NS-P, and NCS-P modified GC electrode. For comparison, commercial RuO2 was also studied under the same conditions. The iR corrected polarization curves in Figure 4a demonstrate that the overpotential required to reach the benchmark current density of 10 mA cm-2 (η10) is quite different among the samples. The as-synthesized NCS-P only needed an overpotential of 273±3 mV to deliver a current density of 10 mA cm−2, which is outperforming that of NS-P (282±2 mV), NCS (300±2 mV), and NS (315±3 mV) (Figure 4b) and also comparable to or even better than most of the reported state-of-the-art non-noble-metal OER catalysts in alkaline media (Table S1), e.g. CoS-doped β-Co(OH)2@Amorphous MoS2+x (380 mV),[26] Co-Mo-S/CC (300 mV),[27] and NF@NiMoCo (277 mV),[28] displayed superior OER activity. Notably, the PANI doped NS and NCS hybrid catalysts (i.e., NS-P and NCS-P) exhibit much lower overpotential than commercial RuO2 (η10 of 290±2 mV), which implied PANI play an important role in the OER process (Figure 4b). Due to the change in oxidation state of Ni from Ni(II) to Ni(III), an anodic peak ~1.38 V vs. RHE appeared in the linear sweep voltammetry (LSV) curves of the all Ni containing catalysts in this work (Figure 4a). To evaluate the enhanced OER activity, the mass activity of obtained catalyst was calculated as follows:

$$Mass\ Activity = \frac{j}{m} \qquad\qquad (1)$$

where j is current density, m is the mass of catalyst loading. With incorporating of PANI, the NCS-P catalyst demonstrate the significantly higher mass activity (155 A g-1), which is ~2.8, ~5.2, and ~8.6 folds higher than those of NS-P (55 A g-1), NCS (30 A g-1), and NS (18 A g-1), respectively, and over an

order of magnitude better than RuO2 (~47 A g-1), a leading precious metal oxide benchmark catalyst (Figure S4).

The Tafel slope is also an inherent characteristic of any electrocatalysts, which can reflect the change rate of current density with increase of overpotentials. Simply, a smaller Tafel slope generally signifies that small overpotential is enough to achieve estimated current density. The Tafel slope of NCS-P is 42.2 mV dec−1 (Figure 4c), which is significantly lower than the Tafel slopes of NS-P (72.4 mV dec−1), NCS (71.8 mV dec−1), NS (78.8 mV dec−1), and RuO2 (69.1 mV dec−1), reflecting outstanding intrinsic OER kinetics and faster oxygen evolution on NCS-P catalyst. The amount of transferred electron for every active site per second should be determined in terms of the turnover frequency (TOF) to better compare the intrinsic OER activity of the various electrocatalysts. However, it is hard to exactly determine the number of active sites in our bi-metallic complex heterostructures, and therefore the TOF is not provided here.

These results demonstrate that the OER kinetics was activated by the coupling interfaces. Table S1 summarizes the OER activity of NCS-P and some of the previously reported catalysts for comparison. It is seen that the NCS-P catalyst exhibits an outstanding OER activity in comparison to the recently reported OER catalysts.

The electrochemically active specific area (ECSA) of the prepared catalysts were determined based on electrochemical double-layer capacitance (Cdl) measured on the basis of the slope from the linear fitting of cyclic voltammogram with the potential ranging from 0.965 0.97 to 1.065 1.07 V vs. RHE at different scanning rates (5 to 50 mV s-1) (Figure S5). As shown in Figure 4d, the Cdl of NCS-P was determined to be 41.8 mF cm-2, much higher than that of NS-P (19.7 mF cm-2), NCS (11.7 mF cm-2), and NS (4.6 mF cm-2), demonstrating that the NCS-P could afford much larger electrochemically active surface area with more active sites, thus contributing to the highest OER performance.

The charge transfer resistance (Rct) of catalysts were further investigated by electrochemical impedance spectroscopy (EIS) measurements. All impedance spectra were fitted using an equivalent circuit model consisting of solution resistance (Rs) and charge-transfer resistance (Rct) in parallel with the constant-phase element (CPE), as shown in Figure S6. Figure 4e shows the corresponding Nyquist plots, in which the high- and low-frequency responses can be attributed to the solution resistance (Rs) and interfacial charge-transfer resistance (Rct) during OER, respectively. Notably, the Rct of NCS-P catalyst is much smaller than other controls, thus confirming the fastest charge transfer in NCS-P during the OER (Figure 4e). The accelerated charge transfer speed of NCS-P not only improved the reaction efficiency but also provoked the effective electrical integration to reduce parasitic ohmic loss, benefiting the whole water splitting process.

Considering that stability is an essential criterion for the large-scale application of electrocatalysts, it can be observed from Figure 4f, NCS-P was relatively stable during the durability test for 24 h, finally preserving 96% of the original current density. The polarization curve after 1000 continuous cyclic voltammetry (CV) scans was conducted, showing a negligible change, indicating the excellent stability of the NCS-P (inset of Figure 4f). In addition, XRD patterns of NCS-P after OER test exhibited non-observable change compared to the pristine NCS-P, which confirms the stability of NCS-P (Figure S7). Though the harsh environment (an alkaline medium) constantly invades the NCS-P material, demonstrating its great potential in practical applications.

Based on the above results, we attributed the enhancement of intrinsic OER performance of the NCS-P to various factors: i) The various valence state of Ni and Co cations in NCS were strictly integrated with larger S^{2-} anions to form a spinel crystal structure (Ni in the tetrahedral sites and Co in the octahedral sites of the spinel structure) (Scheme 1c), which increased the density of OER active sites.[29] ii) Thanks to electronic interaction between NCS and PANI, the high valence metal ions of Ni and Co, responsible for efficient OER catalyst, can be easily

formed at a very low activation potential. iii) The excellent electrophilicity of NCS due to the high valences of Co and Ni were promising for the adsorption of O atoms, further promoting the reaction of OH− with the adsorbed O atoms to form −OOH species for the enhanced OER activities.[23] iii) The improved conductivity caused by the PANI layer on the surface of NCS was beneficial for enhancing the OER activity, because of the rapid ionic and charge transport during the OER reaction.[24] iv) The formation of PANI layer increases the electrochemical surface area of the catalyst, and the conducting layer is expected to provide more active sites for the electrocatalytic reaction which makes the catalyst more efficient for OER.[24]

2.3. Electrocatalytic activity of NCS-P toward HER

Furthermore, development of HER electrocatalysts with excellent catalytic activity in alkaline electrolyte is vital for the sustainable future of various renewable technologies. Most HER catalysts developed to date are efficient in acidic environment. Specifically, reducing high overpotentials and improving the sluggish HER kinetics in alkaline media are the current focus for sustainable development of alkali electrolyzers. In this regard, the HER catalytic activity of the NCS-P with reference to NS, NCS, NS-P, and commercial Pt/C electrocatalysts were studied in 1.0 M KOH at a scan rate of 2 mV s-1 using a conventional three-electrode system and the results were shown in Figure 5a. As shown in Figure 5b, overpotentials of 168±4, 107±4, 124±5, and 77±4 mV are required to achieve a specific current density of -10 mA cm−2 ($\eta 10$) for NS, NCS, NS-P, and NCS-P, respectively. Interestingly, the HER performance of the pristine NS ($\eta 10$ = 168±4 mV) and NCS ($\eta 10$ = 107±4 mV) are significantly improved after introducing PANI, demonstrating the PANI has a substantial effect on the HER catalytic performance of the resulting NS-P ($\eta 10$ = 124±5 mV) and NCS-P ($\eta 10$ = 77±4 mV), respectively.

In general, the addition of PANI into the NS and NCS lattice may induce the presence of multiple valences of the cations with higher electrical conductivity and more complex electronic

structure, which helps to promote the dynamics behavior for proton adsorption and facilitate the H–H bond formation.[18, 30] Impressively, NCS-P exhibits superior HER performance, as expressed by η10 values as low as 77±4 mV. Although the η10 value for NCS-P is higher than that for the commercial Pt/C (η10 = 57±3 mV), the catalytic performance of NCS-P below η10 is better than Pt/C. Note that, the overpotential of our NCS-P is still superior to recently reported noble metal-free HER electrocatalysts (Table S2), demonstrating one of the best reported HER catalysts in an alkaline media. The above results suggest that the existence of PANI dopants, the NS and NCS phases could trigger more HER active sites facilitating charge transfer among the PANI, Ni, and Co in the NS-P and NCS-P composites. To understand better the electrocatalytic effect toward HER the Tafel plots were produced in Figure 5c using polarization curves. As presented in Figure 5c, a Tafel slope of 68.5 mV dec-1 was observed for the NCS-P, which is definitely smaller than those of NCS (93.2 mV dec-1), NS-P (107.1 mV dec-1), and NS (111.3 mV dec-1) but slightly higher than the Tafel slope of commercial Pt/C (65.2 mV dec-1). The Tafel results indicated that the NCS-P catalyst displayed favorable catalytic kinetics.
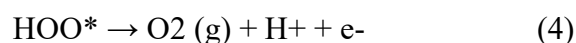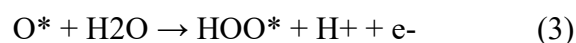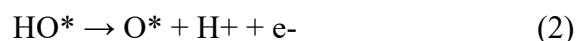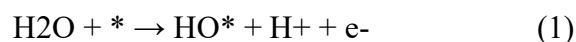
Beyond the electrocatalytic activity, durability is another important standard for the commercial use of the electrocatalysts. To evaluate the long-term stability, we carried out CV experiments for the NCS-P catalyst in alkaline conditions. The polarization curves obtained from CV show an insignificant decrease in performance even after 1000 cycles (Figure 5d), confirming the long-term stability of this catalyst. In addition, the stability of NCS-P was also confirmed by maintained XRD patterns of NCS-P after HER test (Figure S7). The mechanism of the HER by transition metal catalysts in alkaline media can be divided into two steps.[31] The first step is the Volmer reaction or rate-determining step, which involves the adsorption of one proton on the catalytic sites (M) reacts with an electron to form an adsorbed hydrogen atom (Had) on the surface of the electrocatalyst: $H_2O + M + e- \leftrightarrows M - H_{ad} + OH-$. decomposition of H3O+ on the surface of the active catalyst and the formation of adsorbed hydrogen: H3O+

+ e− + M ⇋ M − Had + H2O. The second step may have two pathways including Heyrovsky reaction and Tafel reaction. In Heyrovsky reaction, the adsorbed hydrogen atom combines with H2O and an electron to form a hydrogen molecule: M − Had + H2O + e− ⇋ M + H2 + OH−. The other pathway is the Tafel reaction, where the two adsorbed hydrogen atoms directly attached to produce to form a hydrogen molecule: 2M − Had ⇋ 2M + H2 Had + Had ⇋ H2. Mechanistic studies have suggested that H2 forms via the Volmer–Heyrovsky or Volmer–Tafel pathway. NCS-P showed a Tafel slope of 68.5 mV dec-1, demonstrating that the catalyst followed the Volmer–Heyrovsky mechanism during the HER process.[31]

2.4. The study of the mechanism for enhanced OWS activity by decorating PANI on NCS

To understand the superior activity of the NCS-P for both OER and HER, we performed spin-polarized density functional theory (DFT) calculations. We modeled the NCS and NCS-P surfaces as shown in Figure 6a and 6b (see the Experimental Methods for details) and investigated the most stable adsorption configurations of reaction intermediates on each surface.

In general, OER pathways consist of four- proton-coupled electron transfer (PCET) steps (1-4) as follows:

$$H2O + * \rightarrow HO* + H+ + e- \qquad (1)$$

$$HO* \rightarrow O* + H+ + e- \qquad (2)$$

$$O* + H2O \rightarrow HOO* + H+ + e- \qquad (3)$$

$$HOO* \rightarrow O2\ (g) + H+ + e- \qquad (4)$$

where * represents the catalyst surface and HO*, O*, and HOO* indicates the intermediates adsorbed on each surface. As shown in Figure 6c, all elementary reactions are endothermic and the third PCET step leading to formation of HOO* is the potential-determining step (PDS) for OER on the both NCS and NCS-P surfaces. NCS-P could more strongly stabilize the HOO* intermediate and therefore substantially reduce the energy required for PDS (ΔEPDS) to 3.20

eV, compared with NCS (ΔEPDS=3.42 eV). Additional Bader charge analysis[32] reveals that the net atomic charge of HOO* on NCS and NCS-P surfaces are -0.41 and -0.49, respectively and it indicates NCS-P facilitate more electron transfer from surface to HOO* than NCS by 0.08 e-, thereby promoting OER. This manifests that NCS-P possesses better activity for OER, in good agreement with the experimental results.

The DFT-calculated reaction free energy diagram for HER supports that adding PANI dopant on the NCS enhances the activity for HER. As shown in Figure 6d, HER is limited by the H adsorption (H*) on the both NCS and NCS-P surfaces, however the reaction free energy of H* adsorption is much lower on NCS-P (0.10 eV) than that on the NCS (0.17 eV) which rationalize the HER performance trend in the experiment. Interestingly, it was found that the S atoms on the both NCS and NCS-P surfaces become the H* adsorption sites.

In addition, density of states (DOS) analysis was carried out to obtain further insight into the effect of PANI on the electrical conductivity. The DOS of both NCS and NCS-P surfaces are shown in Figure S8 and notably, the DOS around the Fermi energy level of NCS-P is larger than that of the NCS, which is relevant to enhancement in electron conduction.

2.5. Electrocatalytic activity of NCS-P toward overall water splitting

Triggered by the excellent activity and durability of the NCS-P for both OER and HER in alkaline media, it was highly desirable that the practical water splitting performance to be examined by using home made two-electrode configurations with the NCS-P as both cathode and anode simultaneously as a bifunctional electrocatalyst for the water oxidation and water reduction in 1.0 M KOH solution as the medium (Figure 7a). Owing to its favorable conductivity, porous 3D structure, low price, the Ni-foam (NF) was employed for loading the NCS-P (~1 mg cm-2) and acted as both cathode and anode electrode.[33] As shown in Figure 7b, the LSV curve of NCS-P || NCS-P couple at a scan rate of 5 mV s-1 displayed outstanding OWS performance with a preferably low cell voltage of 1.582 V to attain a stable current

density of 10 mA cm-2, which is far better than most other non-noble metal-based bifunctional water splitting electrocatalysts reported recently (Table S3). Also, NCS, NS-P and NS were used as control samples under the same conditions (Figure S9). The bare NF (without catalyst loading) was also measured to rule out the possible influence of Ni in the NF (Figure 7b). It is noteworthy that the OWS performance of the NCS-P is also outstanding to that of the electrolyzers assembled by commercial Pt/C and RuO2 couple electrocatalysts reported earlier.[33] The apparent H2 and O2 gas bubbles generated could easily be observed on the surface of the cathode and anode electrodes, respectively, reflecting the high HER and OER activities of the NCS-P (inset of Figure 7c and Figure S10). The energy efficiency of the NCS-P ‖ NCS-P couple cell can be calculated using the following equation:

$$\eta\text{electrolyzer} = \frac{E_{th}}{V_i},\qquad\qquad(5)$$

where Eth = 1.23 V and Vi is the input cell voltage required to achieve the current density of 10 mA cm-2. The energy efficiency was estimated to be ~80%, which is comparable to the recently reported values.[3, 34]

In addition, the symmetric two-electrode water-splitting cell revealed the current density of the NCS-P ‖ NCS-P couple still maintain 95.0 % of its initial value at a driving cell voltage of 1.59 V during 48 h of stability test (Figure 7c), which corroborated that the NCS-P composite was highly efficient and stable as the bifunctional electrocatalyst for OWS. The long-term durability of the NCS-P electrocatalyst for OWS is further proven by measuring the LSV curve and the obtained curve was compared with the initially obtained polarization curve (Figure 7d). The change of the LSV curve after 48 h of chronoamperometry measurements is negligible (Figure 7d), thus showing the excellent long-term operational efficiency of the electrocatalyst for OWS. However, the current density retention for the NCS ‖ NCS couple continuously decreased and reached to 75.8% of initial current density after 48 h, showing instability of pristine NCS without the passivation of PANI (Figure S11). As far as we knew, the NCS-P is

one of the best electrocatalysts for OWS by comparing the cell voltages required to reach a current density of 10 mA cm−2 for various non-noble metal bifunctional catalysts (Figure 7e); the information was collected from the literature.[23, 35-43] Therefore, the pair of NCS-P || NCS-P as a two-electrode alkaline electrolyzer exhibits a potential prospect in the application of massive water splitting.

3. Conclusion

In summary, conductive PANI decorated hierarchical thiospinel NCS as a novel electrocatalyst was successfully constructed via a facile hydrothermal process. Coating with the conducting PANI network not only enhances the catalytic kinetic but also prevents the NCS nanoparticles from aggregation to help expose active sites. The catalyst exhibits high activity for both the OER and HER in 1.0 M KOH solution. By comparison, we found that the NCS-P hybrid catalyst exhibits the most superior oxygen evolution activity with the low overpotential of 273±3 mV at the current density of 10 mA cm−2, which exceeds the commercial RuO2 (η = 290±2 mV @ 10 mA cm−2). DFT analysis demonstrates that the incorporation of PANI into thiospinel NCS effectively stabilizes the key intermediate (HOO*) and leads to the enhanced catalytic activity toward OER. In addition, the NCS-P shows excellent hydrogen evolution performance (η = 77±4 mV @ 10 mA cm−2) with outstanding stability (up to at least 1000 cycles) in alkaline media, which is close to that of the benchmark Pt/C electrode (η = 57±3 mV @ 10 mA cm−2). Moreover, the NCS-P electrodes were assembled both as cathode and anode in 1.0 M KOH in a two-electrode cell for real water electrolysis. The tandem NCS-P bifunctional electrocatalyst electrode required a low applied voltage of only 1.582 V to reach a current density of 10 mA cm−2 to realize OWS and maintained at a steady state for at least 48 hours with only 5 % initial current loss. Considering the promising bifunctional electrocatalytic activity, good durability, and the simple synthesized approach, we believe that the NCS-P

catalyst holds great potential in the fields of electrocatalysis and energy conversion technologies.

4. Experimental Section

4.1. Synthesis of electrocatalysts

Materials: Cobalt(II) nitrate hexahydrate ($Co(NO_3)_2 \cdot 6H_2O$) (98.0%), ammonium fluoride (NH_4F) (99.0%), sodium sulfide nonahydrate ($Na_2S \cdot 9H_2O$), and urea (99.0%) were obtained from Samchun Chemicals. Ruthenium (IV) oxide (RuO_2), Pt/C (20 wt % Pt on Vulcan XC-72R), and Nafion (5 wt %) were purchased from Sigma-Aldrich. All the materials for electrochemical measurements were of analytical grade and used without further purification. Deionized (DI) water was used throughout all experiments.

Synthesis of $NiCo_2S_4$ (NCS) and Ni_3S_2 (NS) electrocatalysts: In a typical hydrothermal procedure for preparing NCS catalyst, a solution of ($Ni(NO_3)_2 \cdot 6H_2O$) and ($Co(NO_3)_2 \cdot 6H_2O$) was prepared in 50 mL of DI water with magnetic stirring for 30 min. Urea was added to this solution as a reducing hydrolysis agent with stirring and then the mixture was stirred for another 15 min to obtain a clear solution. The ratio of ($Ni(NO_3)_2 \cdot 6H_2O$) : ($Co(NO_3)_2 \cdot 6H_2O$) : urea was kept the same as 1 : 2 : 4 for the entire experiment. This mixed solution was transferred into Teflon-lined stainless-steel autoclave. The autoclave was locked tightly and placed at 120 °C for 10 h in an electric oven. After being cooled naturally to room temperature, the precipitate was collected by centrifugation at 4000 rpm for 8 min, washed with DI water and ethanol several times, and dried at 60 oC overnight under vacuum.

A sulfide precursor solution was prepared by adding 0.2 M sodium sulfide flakes into 30 mL DI water while stirring for 20 min. This sulfide precursor solution was transferred into an autoclave containing the above Ni-Co powder and maintained at 150 °C for 8 h in an electric drying oven. After cooling to room temperature, the solution was centrifuged at 4000 rpm for 10 min and further subsequently washed with DI water and ethanol to remove any unreacted residues, followed by drying at 60 °C overnight in the vacuum condition. The obtained NCS

samples are denoted as NCS. For comparison of catalytic activities, Ni3S2 was prepared using the same procedure and parameters, but without the cobalt precursor and denoted as NS.

Synthesis of PANI/NiCo2S4 (NCS-P) and PANI/Ni3S2 (NS-P) electrocatalysts: 100 mg of the as-prepared NCS was dispersed in 50 mL ethanol with intense ultra-sonication and stirring. Then, 20 mg of PANI (Laboratory synthesized, detail synthesis procedure and FT-IR analysis are provided in experimental section of the ESI file and Figure S1a) was added and stirred for 5 h. PANI-modified NCS was obtained by centrifugation and washed with DI water and ethanol. Finally, the PANI/NCS was heated at 60 oC for 8 h under vacuum condition and denoted as NCS-P. Scheme 1(a,b) illustrates the preparation and intermediate steps during the formation of NCS and NCS-P. Moreover, PANI/Ni3S2 was prepared through a similar procedure using as-prepared NS instead of NCS and denoted as NS-P.

4.2. Materials characterization

Physicochemical characterization: The phase and structure of samples were studied by X-ray diffraction (XRD) (Rigaku D-MAX/A diffractometer, CuKα radiation, wavelength λ = 0.154 nm). The morphology of the catalysts was observed using field emission scanning electron microscopy (MERLIN Compact, ZEISS) at 1 kV.

The transmission electron microscopy (TEM) and elemental mapping images by energy-dispersive X-ray spectrometry (EDS) were conducted using a Titan G2 6020 transmission electron microscope with accelerating voltage of 200 kV. TEM samples were dissolved in ethanol solution with strong ultrasonic process and deposited on a Quantifoil Cu grid (300 mesh holey carbon). X-ray photoelectron spectra (XPS) were acquired to examine the surface chemical compositions and valence states of elements on an ESCSLAB MK II X-ray photoelectron spectrometer with Mg Kα as the excitation source.

4.3. Electrochemical analysis

Fabrication of electrode and electrochemical measurements: Electrochemical measurement for HER and OER performances were studied using a standard three electrode system working in IVIUMSTAT electrochemical workstation. A glassy carbon electrode with a diameter of 3 mm was used as the working electrode, saturated calomel electrode (SCE) as the reference electrode, a graphite rod and a Pt-mess as the counter electrodes for HER and OER, respectively. For electrochemical tests, the catalyst ink was prepared by ultrasonically dispersing 2.5 mg of catalyst into 1 mL of water/isopropanol (2:1 v/v) mixture containing 50 µL of 5 wt% Nafion (used as a proton conducting binder) and sonicated for 30 minutes to form a homogeneous catalyst ink. To modify the working electrode, 10 µL of the catalyst ink was dropped on the glassy carbon electrode and dried to cover the active area of the electrode. The final loading for all the catalysts on the glassy carbon electrode is about 0.33 mg cm-2.

Additionally, commercial RuO_2 and 20 wt % Pt/C were deposited on the working electrode with the same loading and tested using a similar approach for OER and HER, respectively under identical conditions as reference catalysts for comparison. The HER and OER tests were conducted at room temperature with 1.0 M KOH aqueous solution (pH = 13.6). Before electrochemical analysis, the electrodes were activated by continuous CV cycling for 50 cycles at a scan rate of 10 mV s−1. All the polarization curves for HER and OER were recorded using LSV measurements at a sweep rate of 2 mV s−1 in the potential region from 0.15 to −0.5 V vs. RHE (for HER) and 1.0 to 1.8 V (vs. RHE) (for OER) with 95% iR correction. Then the iR-corrected data is given by $E_{corr} = E_{mea} – iR_u$, where E_{corr} is the iR-corrected potential, E_{mea} is the experimentally measured potential, and R_u is the uncompensated resistance. The electrochemical impedance spectroscopy (EIS) measurements were carried out in the frequency range of 0.01 to 105 Hz under a bias of +0.55 V (OER) in 1.0 M KOH aqueous solution with an AC voltage amplitude of 5 mV, respectively, under open circuit conditions. The long-term stability tests of the electrocatalysts were carried out by comparing the LSV data before and after 1000 cycles of CV test with iR-correction. All the potentials were converted to the reversible hydrogen electrode (RHE) with 1.0 M KOH electrolyte according to the Nernst

equation (ERHE = ESCE + 0.242 + 0.059 × pH). The overpotential (η) values were measured from η = ERHE −1.23 V, for OER and η = ERHE − 0 V for HER. Chronopotentiometry was conducted at a constant current density of 10 mA cm−2 (for OER) or −10 mA cm−2 (for HER). The Tafel slopes were calculated by the Tafel equation η = b ×log (j/j0), where η is the overpotential for OER or HER, b is the Tafel slope, and j0 is the exchange current density.

CV was conducted to evaluate the electrochemical double-layer capacitance (Cdl) and the electrochemical surface area (ECSA) at different scan rates of 5, 10, 15, 20, 25, 30, 35, 40, 45, and 50 mV s−1 with the potential of non-faradaic current observed. The electrolyte solution was vigorously stirred by a magnetic stirring bar to remove the generated gas bubbles and promotion of mass transport during the chronoamperometry (CA) measurements.

At least four electrodes were prepared using every catalyst to ensure the reproducibility of our experimental results. For the OWS measurement, 250 µL of two identical catalysts ink were dipped onto two Ni-foams (1×1 cm2) to achieve the mass loading of ~1 mg cm-2. After naturally dried in air, the two identical working electrodes were used as both the anode and cathode. Polarization measurements were carried out in a O2-saturated 1.0 M KOH solution at a scan rate of 5 mV s-1 to evaluate the OWS performance without iR corrections under room temperature.

4.4. Computational details

Spin-polarized density functional theory (DFT) calculations were performed using the Vienna Ab-initio Simulation Package[44] to provide insight into the origin of high OER and HER activity on the PANI-modified surfaces. Perdew-Burke-Ernzerhof (PBE) exchange-correlation functional[45] coupled with the D3 correction[46] for London dispersion and the projector augmented wave (PAW) method[47] were employed. In addition, implicit solvation model was used to consider the solvation effect as implemented in VASPsol.[48] To calculate the free energy change in both OER and HER steps, the zero-point energy and entropy at 298.15 K were calculated.

For the structural optimization of cubic NCS bulk unit cell, a plane-wave energy cutoff of 600 eV was employed and the reciprocal space was sampled using the (8×8×1) Monkhorst-Pack grid.[49] The calculated equilibrium lattice parameter for NCS (a=9.28 Å) is in good agreement with previous experimental data (a=9.30 Å).[50]

The NCS (100) surface with four-layers were built by cleaving the optimized bulk unit cell and adding a vacuum region of 20 Å and the NCS-P (100) surface was modelled by covering the NCS (100) surface with monomer of PANI, aniline ($C_6H_5NH_2$), as shown in Figure 6a and Figure 6b, respectively. For the optimization of the surface models, a plane-wave energy cutoff of 400 eV and Monkhorst-Pack grid of (1×1×1) were used and dipole correction was applied in the direction perpendicular to the surface layers. The two bottom layers were fixed while the other two layers and adsorbed species were allowed to relax.

Supporting Information
Supporting Information is available from the Wiley Online Library or from the author.

Acknowledgements

References

[1]   Z. W. Seh, J. Kibsgaard, C. F. Dickens, I. Chorkendorff, J. K. Nørskov, T. F. Jaramillo, Science 2017, 355, eaad4998.
[2]   J. A. Turner, Science 2004, 305, 972.
[3]   A. Ursua, L. M. Gandia, P. Sanchis, Proc. IEEE 2012, 100, 410.
[4]   Y. Jiao, Y. Zheng, M. Jaroniec, S. Z. Qiao, Chem. Soc. Rev. 2015, 44, 2060.
[5]   W. T. Hong, M. Risch, K. A. Stoerzinger, A. Grimaud, J. Suntivich, Y. Shao-Horn, Energy Environ. Sci. 2015, 8, 1404.
[6]   C. Tang, W. Wang, A. Sun, C. Qi, D. Zhang, Z. Wu, D. Wang, ACS Catal. 2015, 5, 6956.
[7]   Y. Luo, X. Li, X. Cai, X. Zou, F. Kang, H.-M. Cheng, B. Liu, ACS Nano 2018, 12, 4565.

[8]   D. Tang, J. Liu, X. Wu, R. Liu, X. Han, Y. Han, H. Huang, Y. Liu, Z. Kang, ACS Appl. Mater. Interfaces 2014, 6, 7918.

[9]   Y. Song, J. Cheng, J. Liu, Q. Ye, X. Gao, J. Lu, Y. Cheng, Appl. Catal. B 2021, 298, 120488.

[10]   X.-F. Lu, L.-F. Gu, J.-W. Wang, J.-X. Wu, P.-Q. Liao, G.-R. Li, Adv. Mater. 2017, 29, 1604437.

[11]   J. Chen, G. Xia, P. Jiang, Y. Yang, R. Li, R. Shi, J. Su, Q. Chen, ACS Appl. Mater. Interfaces 2016, 8, 13378.

[12]   D. Wang, Y. Chen, L. Fan, T. Xiao, T. Meng, Z. Xing, X. Yang, Appl. Catal. B 2022, 305, 121081.

[13]   B. You, N. Jiang, M. Sheng, S. Gul, J. Yano, Y. Sun, Chem. Mater. 2015, 27, 7636.

[14]   H. Anwer, H. Lee, H.-R. Kim, H.-K. Kim, J.-W. Park, Appl. Catal. B 2020, 265, 118564.

[15]   R. Chen, H.-Y. Wang, J. Miao, H. Yang, B. Liu, Nano Energy 2015, 11, 333.

[16]   N.-T. Suen, S.-F. Hung, Q. Quan, N. Zhang, Y.-J. Xu, H. M. Chen, Chem. Soc. Rev. 2017, 46, 337.

[17]   C. Xiao, Y. Li, X. Lu, C. Zhao, Adv. Funct. Mater. 2016, 26, 3515.

[18]   S. Chen, Z. Wei, X. Qi, L. Dong, Y.-G. Guo, L. Wan, Z. Shao, L. Li, J. Am. Chem. Soc. 2012, 134, 13252.

[19]   J.-X. Feng, S.-Y. Tong, Y.-X. Tong, G.-R. Li, J. Am. Chem. Soc. 2018, 140, 5118.

[20]   Y. Wen, S. Peng, Z. Wang, J. Hao, T. Qin, S. Lu, J. Zhang, D. He, X. Fan, G. Cao, J. Mater. Chem. A 2017, 5, 7144.

[21]   X. Xiong, G. Waller, D. Ding, D. Chen, B. Rainwater, B. Zhao, Z. Wang, M. Liu, Nano Energy 2015, 16, 71.

[22]   L. Mi, W. Wei, S. Huang, S. Cui, W. Zhang, H. Hou, W. Chen, J. Mater. Chem. A 2015, 3, 20973.

[23]   A. Sivanantham, P. Ganesan, S. Shanmugam, Adv. Funct. Mater. 2016, 26, 4661.

[24]   Y. Zou, Y. Huang, L.-W. Jiang, A. Indra, Y. Wang, H. Liu, J.-J. Wang, Nanotechnology 2022, 33, 155402.

[25]   X. Chen, Y. Chen, Z. Shen, C. Song, P. Ji, N. Wang, D. Su, Y. Wang, G. Wang, L. Cui, Appl. Surf. Sci. 2020, 529, 147173.

[26]   T. Yoon, K. S. Kim, Adv. Funct. Mater. 2016, 26, 7370.

[27]   Y.-J. Tang, A. M. Zhang, H.-J. Zhu, L.-Z. Dong, X.-L. Wang, S.-L. Li, M. Han, X.-X. Xu, Y.-Q. Lan, Nanoscale 2018, 10, 8404.

[28]   K. Hu, M. Wu, S. Hinokuma, T. Ohto, M. Wakisaka, J.-i. Fujita, Y. Ito, J. Mater. Chem. A 2019, 7, 2156.

[29]   X. Zhao, H. Liu, Y. Rao, X. Li, J. Wang, G. Xia, M. Wu, ACS Sustainable Chem. Eng. 2019, 7, 2610.

[30]   J.-X. Feng, L.-X. Ding, S.-H. Ye, X.-J. He, H. Xu, Y.-X. Tong, G.-R. Li, Adv. Mater. 2015, 27, 7051.

[31]   Z. Kang, H. Guo, J. Wu, X. Sun, Z. Zhang, Q. Liao, S. Zhang, H. Si, P. Wu, L. Wang, Y. Zhang, Adv. Funct. Mater. 2019, 29, 1807031.

[32]   G. Henkelman, A. Arnaldsson, H. Jónsson, Comput. Mater. Sci. 2006, 36, 354.

[33]   M. Li, Y. Zhu, H. Wang, C. Wang, N. Pinna, X. Lu, Adv. Energy Mater. 2019, 9, 1803185.

[34]   B. H. R. Suryanto, Y. Wang, R. K. Hocking, W. Adamson, C. Zhao, Nat. Commun. 2019, 10, 5599.

[35]   Y. Hao, Y. Xu, W. Liu, X. Sun, Mater. Horiz. 2018, 5, 108.

[36]   Q. Yuan, Y. Yu, Y. Gong, X. Bi, ACS Appl. Mater. Interfaces 2020, 12, 3592.

[37]   W. Wang, Y. Xu, J. Yao, X. Liu, Z. Yin, Z. Li, Dalton Trans. 2020, 49, 13352.

[38]   P. Wang, Y. Lin, L. Wan, B. Wang, Energy Fuels 2020, 34, 10276.

[39]   C. Kim, S. Lee, S. H. Kim, I. Kwon, J. Park, S. Kim, J.-h. Lee, Y. S. Park, Y. Kim, Nanoscale Adv. 2021, 3, 6386.

[40]   S. She, Y. Zhu, H. A. Tahini, X. Wu, D. Guan, Y. Chen, J. Dai, Y. Chen, W. Tang, S. C. Smith, H. Wang, W. Zhou, Z. Shao, Small 2020, 16, 2006800.

[41]   Y. Huang, X. Chen, S. Ge, Q. Zhang, X. Zhang, W. Li, Y. Cui, Catal. Sci. Technol. 2020, 10, 1292.

[42]   D. Li, Y. Xing, R. Yang, T. Wen, D. Jiang, W. Shi, S. Yuan, ACS Appl. Mater. Interfaces 2020, 12, 29253.

[43]   J. Luo, W. H. Guo, Q. Zhang, X. H. Wang, L. Shen, H. C. Fu, L. L. Wu, X. H. Chen, H. Q. Luo, N. B. Li, Nanoscale 2020, 12, 19992.

[44]   G. Kresse, J. Furthmüller, Phy. Rev. B 1996, 54, 11169.

[45]   B. Hammer, L. B. Hansen, J. K. Nørskov, Phy. Rev. B 1999, 59, 7413.

[46]   E. R. Johnson, A. D. Becke, J. Chem. Phys. 2006, 124, 174104.

[47]   P. E. Blöchl, Phy. Rev. B 1994, 50, 17953.

[48]   K. Mathew, R. Sundararaman, K. Letchworth-Weaver, T. A. Arias, R. G. Hennig, J. Chem. Phys. 2014, 140, 084106.

[49]   H. J. Monkhorst, J. D. Pack, Phy. Rev. B 1976, 13, 5188.

[50]   S. K. Shinde, S. Ramesh, C. Bathula, G. S. Ghodake, D. Y. Kim, A. D. Jagadale, A. A. Kadam, D. P. Waghmode, T. V. M. Sreekanth, H. S. Kim, P. C. Nagajyothi, H. M. Yadav, Sci. Rep. 2019, 9, 13717.
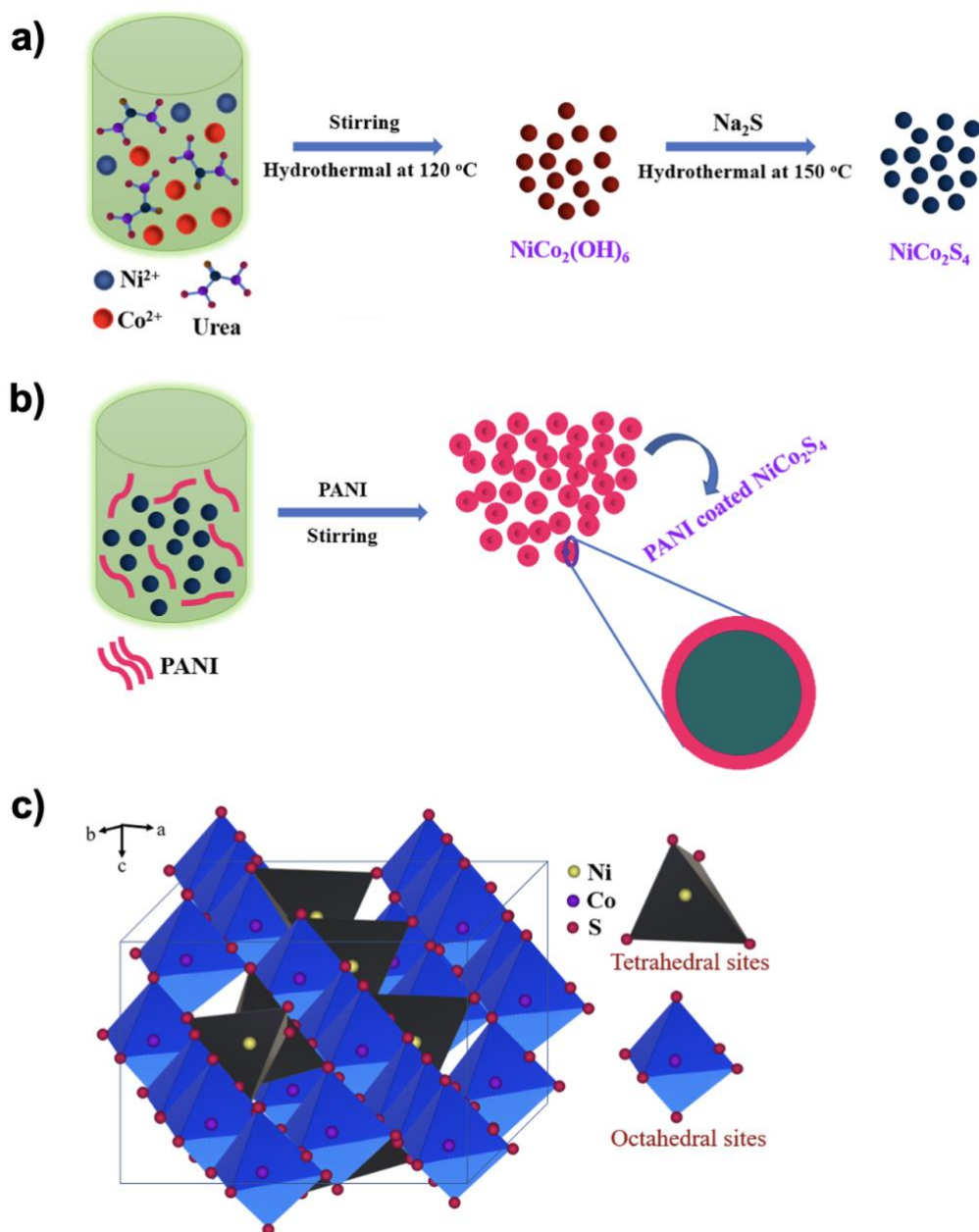
Scheme 1. Schematic illustration of the preparation of hierarchical (a) NCS and (b) PANI coated NCS via hydrothermal method. (c) Spinel-type crystal structure of NCS. Ni cations occupy the tetrahedral sites and Co cations occupy the octahedral sites.
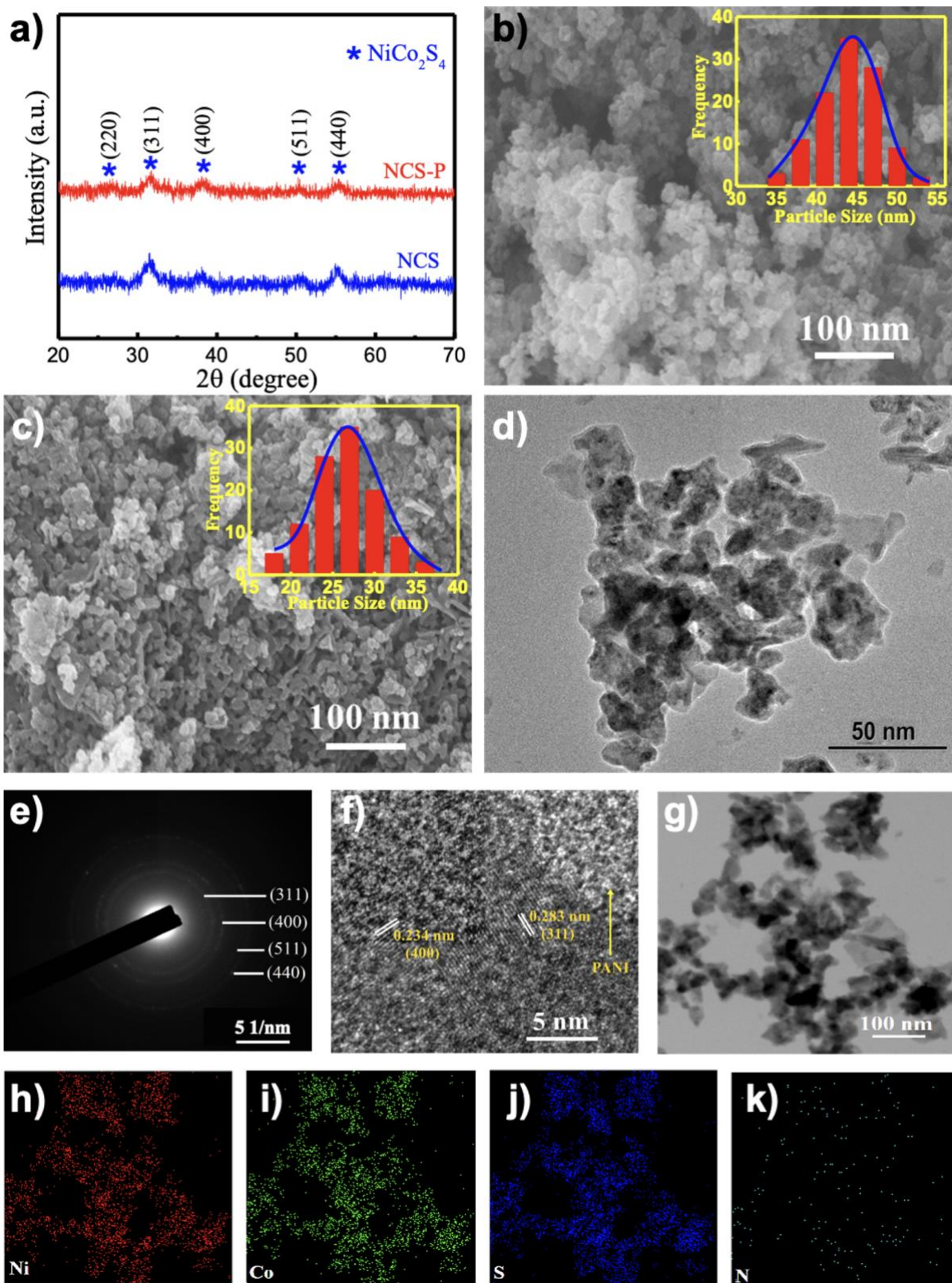
Figure 1. (a) XRD patterns of NCS and NCS-P. FE-SEM images of (b) NCS and (c) NCS-P. (d) TEM image of NCS-P. (e) SAED patterns and corresponding indices of lattice planes. (f) HRTEM image of NCS-P. (g) STEM image and the corresponding EDS elemental mapping of (h) Ni, (i) Co, (j) S, and (k) N taken from NCS-P catalyst. Inset of (b) and (c) represent the particle size distribution curves NCS and NCS-P, respectively.
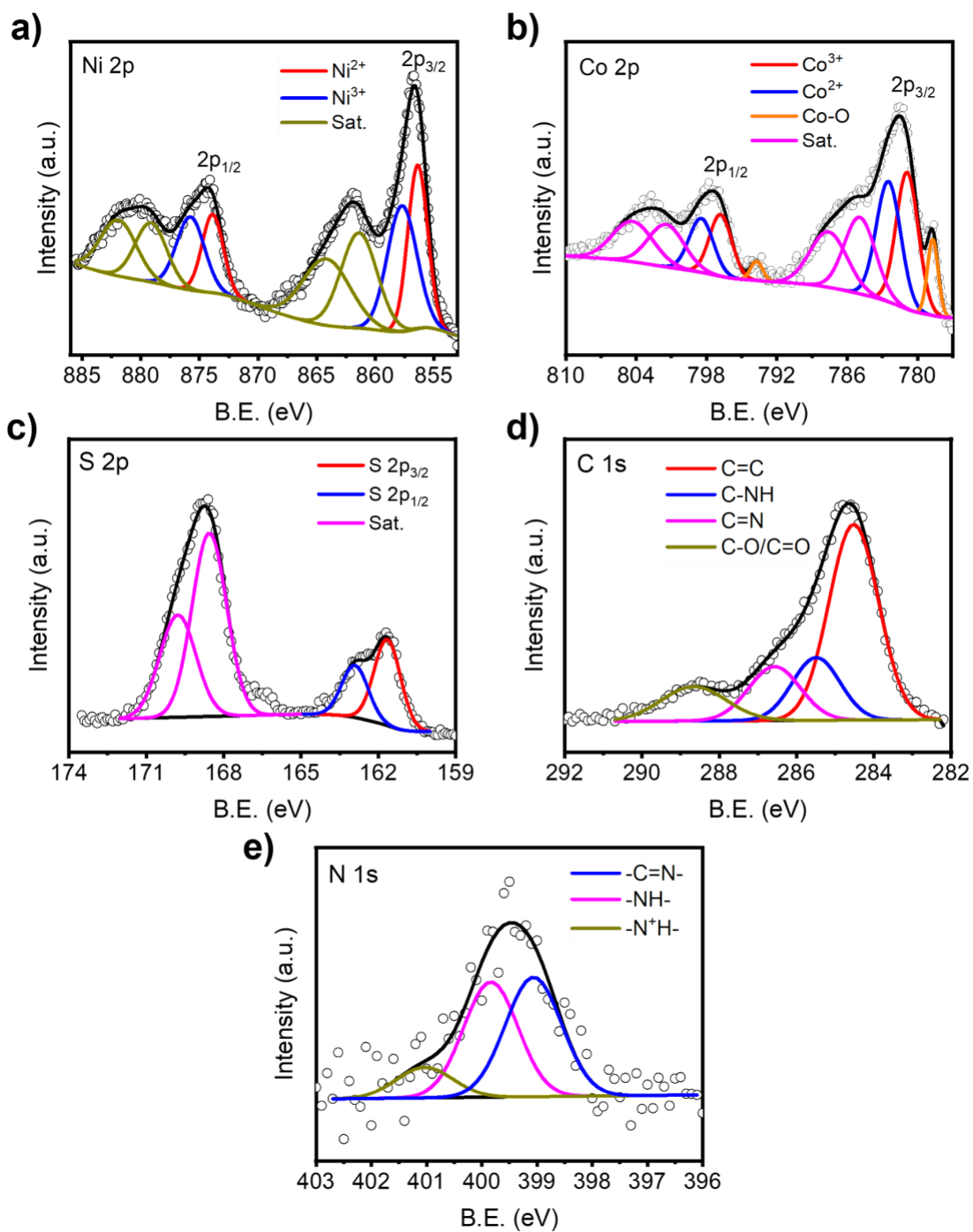
Figure 2. High-resolution XPS spectra of (a) Ni 2p, (b) Co 2p, (c) S 2p, (d) C 1s, and (e) N 1s core-levels for the NCS-P catalyst.
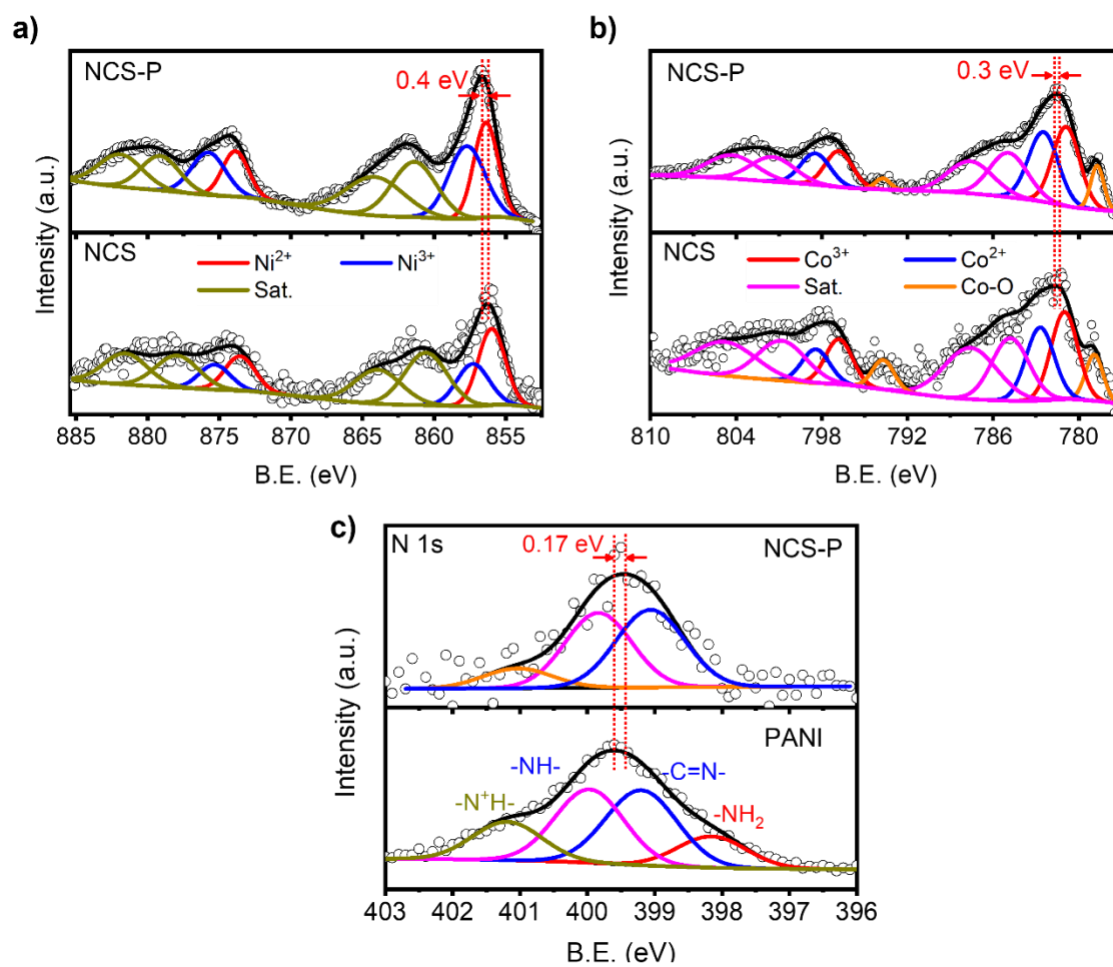
Figure 3. High resolution XPS spectra of (a) Ni 2p and (b) Co 2p for the NCS and NCS-P catalysts. (c) XPS spectra of N 1s region for the PANI and NCS-P.
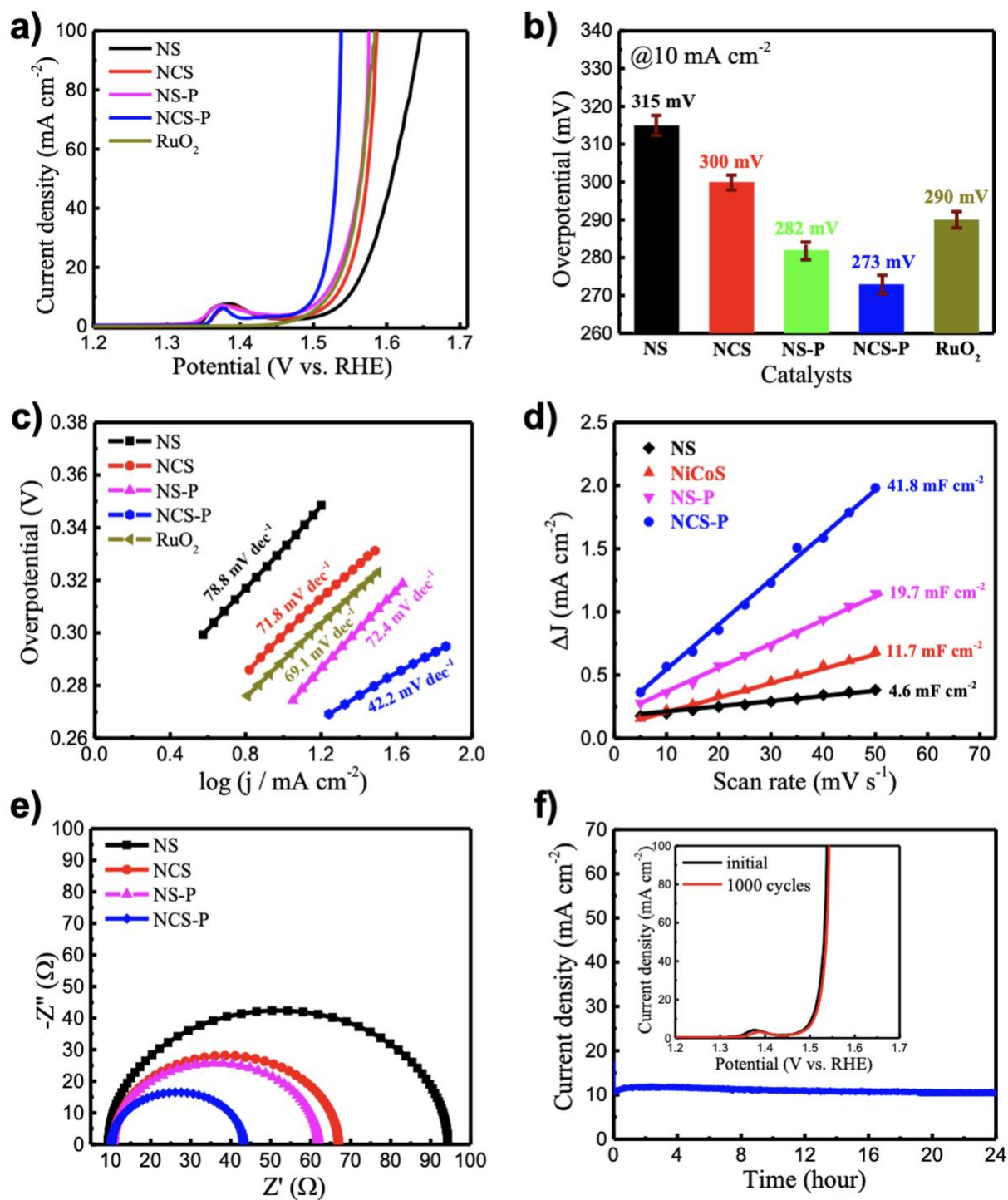
Figure 4. (a) The OER polarization curves of as-prepared catalysts and the commercial RuO2; (b) the overpotentials at 10 mA cm-2 and (c) corresponding Tafel plots of the NS, NCS, NS-P, NCS-P, and commercial RuO2. (d) Nyquist plots of electrochemical impedance spectra (EIS) the NS, NCS, NS-P, NCS-P under an overpotential of 280 mV (vs. RHE); (e) the capacitive current at 1.015 V (vs. RHE) as a function of scan rate for NS, NCS, NS-P, NCS-P. (f) Current density vs. time (I–t) profiles of NCS-P for OER at a constant overpotential of 280 mV and the inset shows the LSV curves of NCS-P before and after 1000 CV cycles to evaluate the stability of the catalyst.
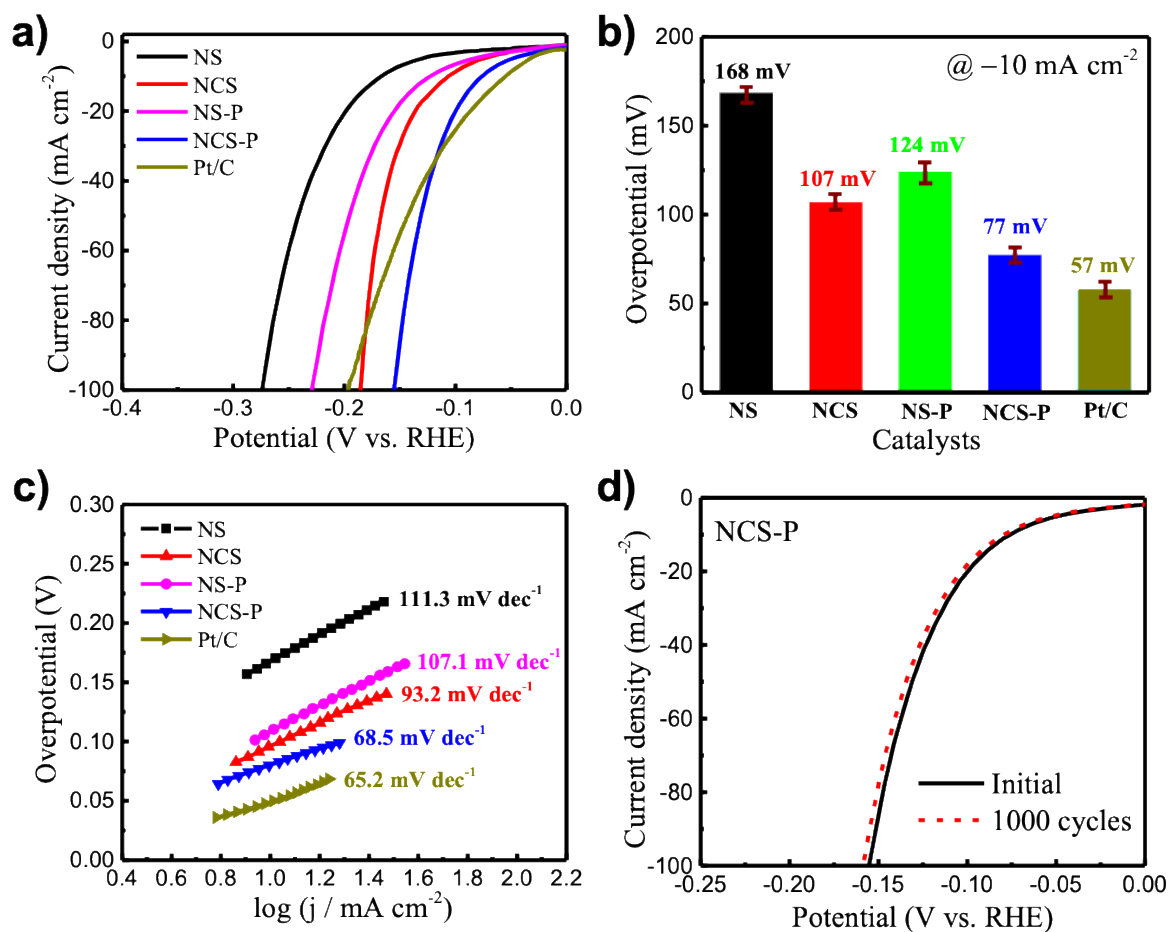
Figure 5. (a) Linear sweep voltammetry (LSV) curves in 1.0 M KOH for NS, NCS, NS-P, NCS-P, and commercial Pt/C, which deposited on a glassy carbon electrode as HER catalysts. (b) Histogram of the overpotentials measured at the current density of -10 mA cm-2. (c) Tafel plots derived from the LSV curves and the number in the parenthesis represents the Tafel slope. (d) LSV curves of NCS-P electrocatalyst in the initial state and after 1000 CV cycles in 1.0 M KOH.
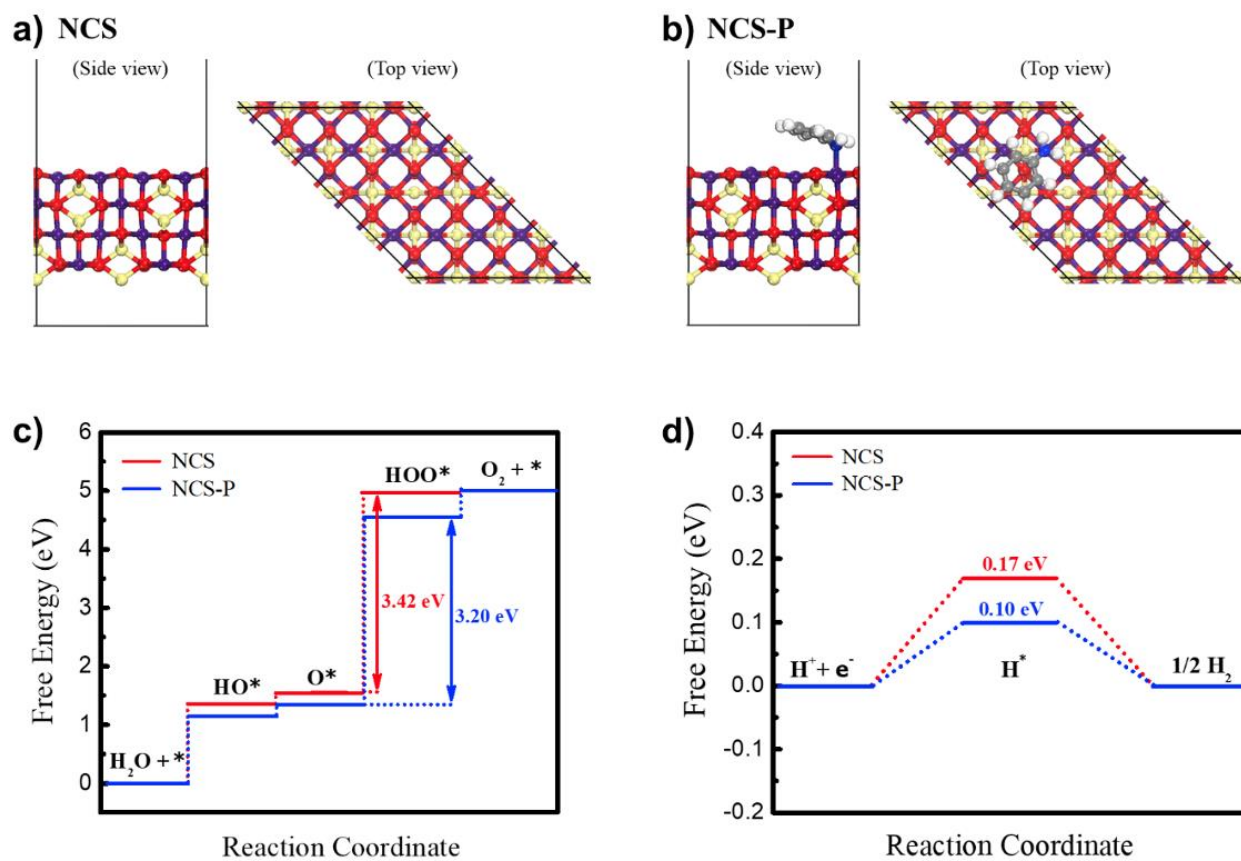
Figure 6. The optimized surface geometries of (a) NCS and (b) NCS-P. Yellow, purple, red gray, navy, and white atoms indicate Ni, Co, S, C, N, and H, respectively. DFT calculated reaction free energy diagrams for (c) OER and (d) HER of NCS (red) and NCS-P (blue).
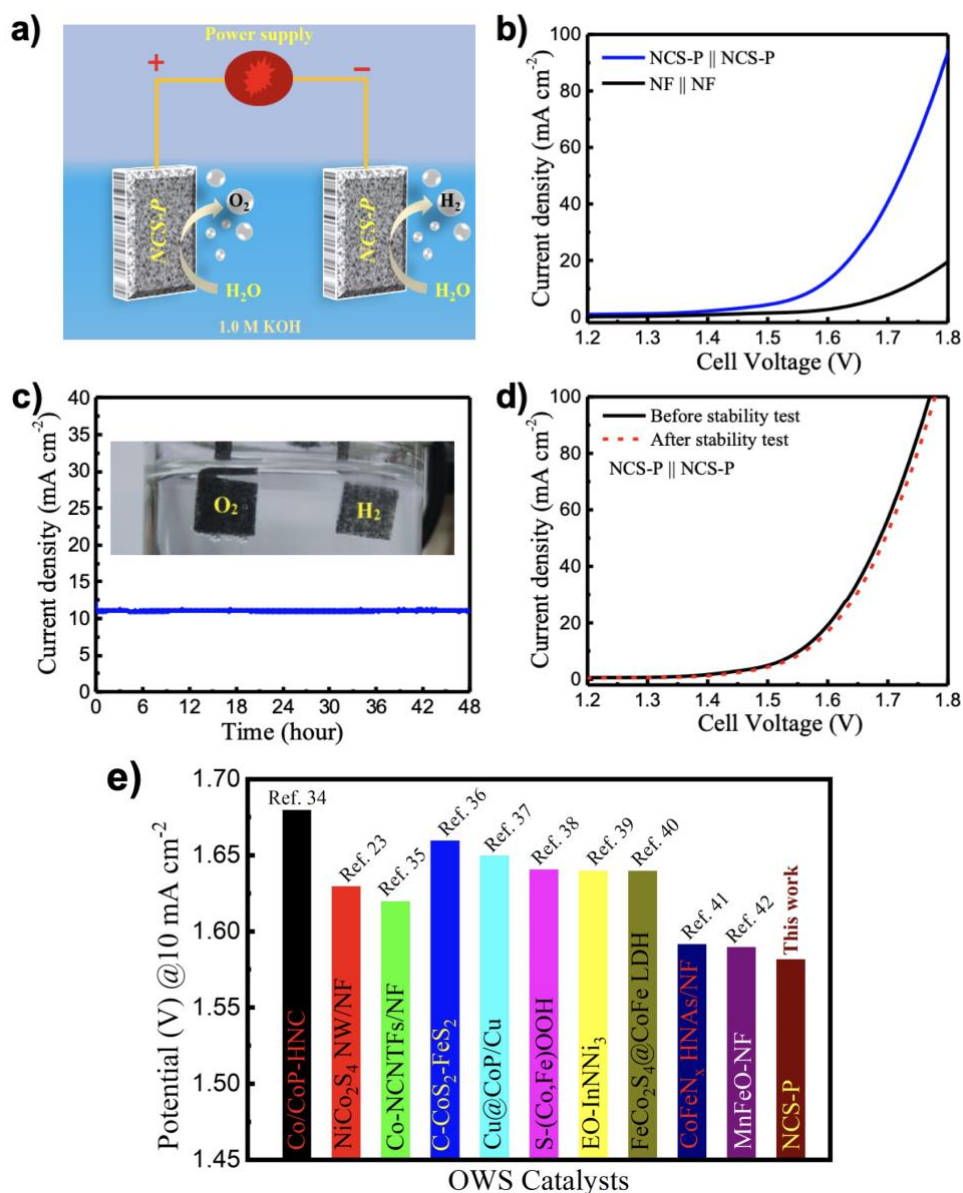
Figure 7. (a) Schematic diagram of the two-electrode configuration for overall water splitting with NCS-P as both anode and cathode in 1.0 M KOH solution. (b) Overall water splitting performance of the NCS-P || NCS-P and bare NF || NF couples in 1.0 M KOH solution. (c) Durability test of the NCS-P || NCS-P electrode at a definite cell voltage of 1.59 V displayed outstanding stability with vigorous bubble formation during the constant-current electrocatalysis process (inset image). (d) Polarization curves of the NCS-P || NCS-P was measured in 1.0 M KOH solution before and after ~48 h durability test. (e) Comparison of the cell voltages at the current density of 10 mA cm-2 for OWS in this work with other recently reported bifunctional electrocatalysts.

A polyaniline (PANI) decorated thiospinel NiCo2S4 hybrid catalyst (NCS-P) with high catalytic performance in both hydrogen evolution reaction (HER) and oxygen evolution reaction (OER) in basic medium is developed. The NCS-P exhibits low overpotentials of 273 mV and 77 mV to achieve a current density of 10 mA cm−2 with low Tafel slope values for OER and HER, respectively, which are better than that of the benchmark noble-metal-based RuO2 catalyst and comparable to that of the commercial Pt/C.

S. Garain, C. Dang Van, S. Choi, T. Nguyen Dang, J. W. Ager, K. T. Nam, H. Shin,* and M. H. Lee*

Hierarchical Thiospinel NiCo2S4/Polyaniline Hybrid Nanostructures as a Bifunctional Electrocatalyst for Highly Efficient and Durable Overall Water Splitting